

1 Direct Evidence of a Graded Magnetic Interface in Bimagnetic Core/ 2 Shell Nanoparticles Using Electron Magnetic Circular Dichroism 3 (EMCD)

4 Daniel del-Pozo-Bueno,* María Varela,* Marta Estrader, Alberto López-Ortega,* Alejandro G. Roca,*
5 Josep Nogués, Francesca Peiró, and Sònia Estradé



Cite This: <https://doi.org/10.1021/acs.nanolett.1c02089>



Read Online

ACCESS |



Metrics & More



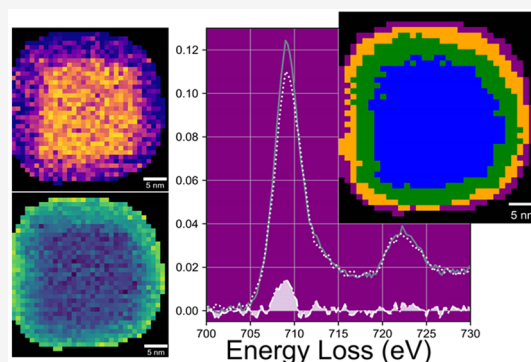
Article Recommendations



Supporting Information

6 **ABSTRACT:** Interfaces play a crucial role in composite magnetic materials
7 and particularly in bimagnetic core/shell nanoparticles. However, resolving
8 the microscopic magnetic structure of these nanoparticles is rather complex.
9 Here, we investigate the local magnetization of antiferromagnetic/
10 ferrimagnetic FeO/Fe₃O₄ core/shell nanocubes by electron magnetic circular
11 dichroism (EMCD). The electron energy-loss spectroscopy (EELS)
12 compositional analysis of the samples shows the presence of an oxidation
13 gradient at the interface between the FeO core and the Fe₃O₄ shell. The
14 EMCD measurements show that the nanoparticles are composed of four
15 different zones with distinct magnetic moment in a concentric, onion-type,
16 structure. These magnetic areas correlate spatially with the oxidation and
17 composition gradient with the magnetic moment being largest at the surface
18 and decreasing toward the core. The results show that the combination of
19 EELS compositional mapping and EMCD can provide very valuable information on the inner magnetic structure and its correlation
20 to the microstructure of magnetic nanoparticles.

21 **KEYWORDS:** EMCD, EELS, Magnetic Nanoparticles, Core/Shell Nanoparticles, Graded Interfaces



22 ■ INTRODUCTION

23 Understanding the interface structure between the different
24 components of nanocomposite structures constitutes the
25 keystone to harness the functional properties of the materi-
26 al.^{1–8} In particular, graded interfaces (where there is some
27 degree of chemical intermixing between the two counterparts
28 at the interface; also denoted as rough or interdiffused
29 interfaces) have been shown to play a critical role in tuning
30 the properties of diverse materials^{1–7} and specifically in core/
31 shell nanoparticles.^{3,9–12} However, despite the paramount
32 importance of interfaces, the process of gaining detailed
33 information about them can be rather complex, since
34 specialized tools must be used to characterize interfaces of
35 core/shell nanoparticles at the atomic level in real space,
36 including compositional information (e.g., transmission elec-
37 tron microscopy, TEM, combined with electron energy-loss
38 spectroscopy, EELS; anomalous small-angle X-ray scattering,
39 SAXS; extended X-ray absorption fine structure, EXAFS; or
40 complex X-ray diffraction analysis).^{11,13–15}

41 The degree of complexity increases in bimagnetic core/shell
42 nanoparticles, a widespread type of core/shell particles due to
43 their remarkable fundamental properties and the broad range
44 of applications. In these systems, both the core and the shell
45 exhibit magnetic properties (i.e., ferromagnetic, ferrimagnetic,

antiferromagnetic).^{3,7,14–16} Here, not only is the structural/
46 morphological interface important but also the magnetic
47 arrangement at the interface (e.g., strength of the exchange
48 coupling, ferromagnetic versus antiferromagnetic interface
49 coupling, graded anisotropy or proximity effects)^{12,17–19} can
50 play a crucial role in the properties and performance of the
51 nanoparticles. However, obtaining information on the interface
52 magnetic structure in nanoparticles is particularly challenging.
53 Indirect information on the magnetic structure at the interface
54 can sometimes be inferred from magnetization, X-ray magnetic
55 circular dichroism (XMCD), Mössbauer spectroscopy, and
56 other techniques.^{20–22} However, these techniques give
57 information on the whole sample, thus their lack of direct
58 spatial resolution precludes establishing a one-to-one correla-
59 tion between the magnetic behavior and the structural/
60 morphological features at the atomic scale. To obtain a
61 straightforward correlation between the structural and 62

Received: May 27, 2021

Revised: July 28, 2021

63 magnetic interface, small angle neutron scattering (SANS) can
64 be used, although it has been used only occasionally in
65 bimagnetic core/shell nanoparticles.^{23,24} However, SANS
66 averages over long lateral distances (typically, the whole
67 sample), thus certain specifics of the structural–magnetic
68 correlation can be easily overlooked. To gain a more
69 microscopic insight of the structural–magnetic interface
70 correlation, high-resolution magnetic transmission electron
71 microscopy techniques like e-holography could potentially be
72 applied, although it has been rarely used to study bimagnetic
73 core/shell nanoparticles.^{25,26}

74 A very specific TEM-based technique to study the magnetic
75 information at an atomic/nanometric length scale is energy-
76 loss chiral magnetic dichroism, or electron magnetic circular
77 dichroism (EMCD).^{27,28} EMCD is based on studying the
78 difference between two EEL spectra acquired under the
79 appropriate scattering conditions inside the TEM.^{27,29,30}
80 Although this approach allows obtaining the local magnetic
81 moment with subnanometer precision, it has seldom been
82 utilized on nanoparticles.^{29,31}

83 Here, we demonstrate that EMCD can disentangle the
84 magnetic properties of iron oxide-based core/shell nanocubes,
85 consisting of a ferrimagnetic magnetite (Fe_3O_4) shell and an
86 antiferromagnetic wüstite (FeO) core. Combining a high
87 spatial resolution (0.45 nm) with clustering techniques for
88 EELS data analysis,³² the existence of a graded magnetic
89 interface, associated with an oxidation gradient between the
90 shell and core, is unambiguously established. It is interesting to
91 note that an in-depth comprehension of the magnetic structure
92 in bimagnetic nanoparticles^{3,16,18,20} and, specifically, in $\text{FeO}/$
93 Fe_3O_4 core/shell systems is essential not only from a more
94 fundamental magnetic point of view but also for the
95 optimization of their magnetic properties for their use in
96 diverse fields like biomedical applications (e.g., magnetic
97 hyperthermia or magnetic bioassays) or microwave absorbers.
98 ^{33–36}

99 ■ RESULTS AND DISCUSSION

100 **Morphological Characterization.** The $\text{FeO}/\text{Fe}_3\text{O}_4$ core/
101 shell nanoparticles, synthesized by thermal decomposition (see
102 Methods in Supporting Information), show a rather regular
103 square shape and a high crystallinity with an average particle
104 size of 29 ± 3 nm (Figure 1a). The core/shell structure was
105 verified by means of annular bright-field (ABF) and annular
106 dark-field (ADF) scanning transmission electron microscopy
107 (STEM) images, evidencing a rather homogeneous morphol-
108 ogy with a shell thickness of about 5–6 nm (Figure 1b,c) along
109 with a cubic shape core, in agreement with previous studies on
110 similar nanoparticles.^{37,38} In contrast to other oxide core/shell
111 nanoparticles,³⁹ it is worth noting that the core/shell structure
112 (and oxidation states; see below) remains very stable under the
113 current imaging conditions (200 kV acceleration voltage, beam
114 currents of tens of pA), even after prolonged electron beam
115 exposure. Pure Fe_3O_4 nanoparticles were also grown by
116 thermal decomposition to serve as a reference. They also show
117 a good cubic morphology with an excellent crystallinity, and
118 the same particle size of 29 ± 3 nm as the $\text{FeO}/\text{Fe}_3\text{O}_4$ core/
119 shell nanoparticles (Figure S1).

120 **Oxidation State and Compositional Analysis.** Figure
121 2a depicts the spatial map of the Fe oxidation state obtained
122 from the distance between the oxygen K edge and the L_3 iron
123 white line (method ii, see Methods in Supporting Informa-
124 tion). Note that the signal at the left-hand side of the image

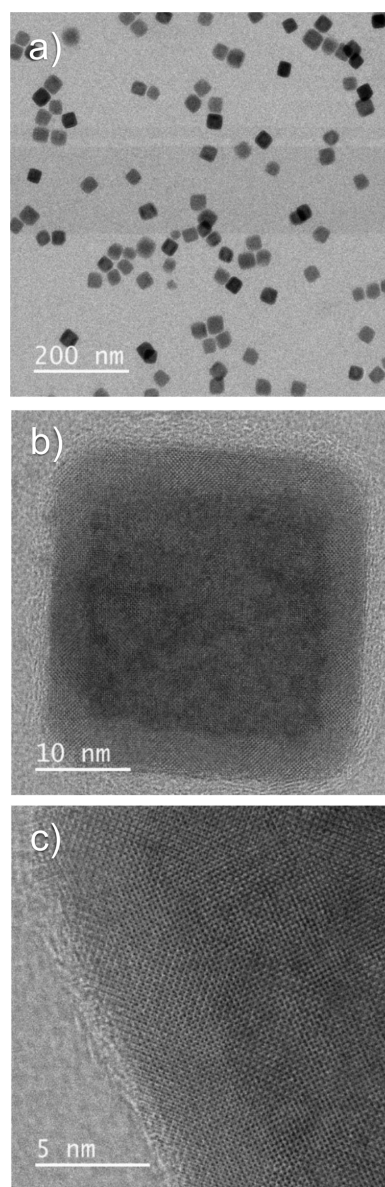


Figure 1. (a) ABF STEM image at low magnification of the $\text{FeO}/\text{Fe}_3\text{O}_4$ core/shell nanocubes. (b,c) ABF STEM images of an individual core/shell nanocube at high magnification.

125 corresponds to a neighboring particle. Although in the image
126 they appear to be in contact, the particles are not overlapping
127 as shown in Figure S2. Additional analysis of the EELS data
128 using alternative calculation approaches^{40–47} are presented in
129 Figures S3a–c. All of the four methods used show very similar
130 results (see Methods in Supporting Information for details).
131 The core/shell structure can be clearly identified in these
132 oxidation state maps. The profile of the oxidation state
133 presented in Figure 2b (left axis) has been calculated from the
134 mean values obtained for the four calculation methods with an
135 additional vertical average within the dotted box in Figure 2a,
136 to improve signal-to-noise ratio. The oxidation state of the
137 shell is close to the expected +2.65 for Fe_3O_4 . On the other
138 hand, within the core regions the value of the oxidation state is
139 closer to +2.2, a value that is larger than the one corresponding
140 to FeO (+2.0). This finding is probably a consequence of the
141 measurements representing a 2D projection of 3D structure of
142 the particles, that is, the shell covering the core. Since the

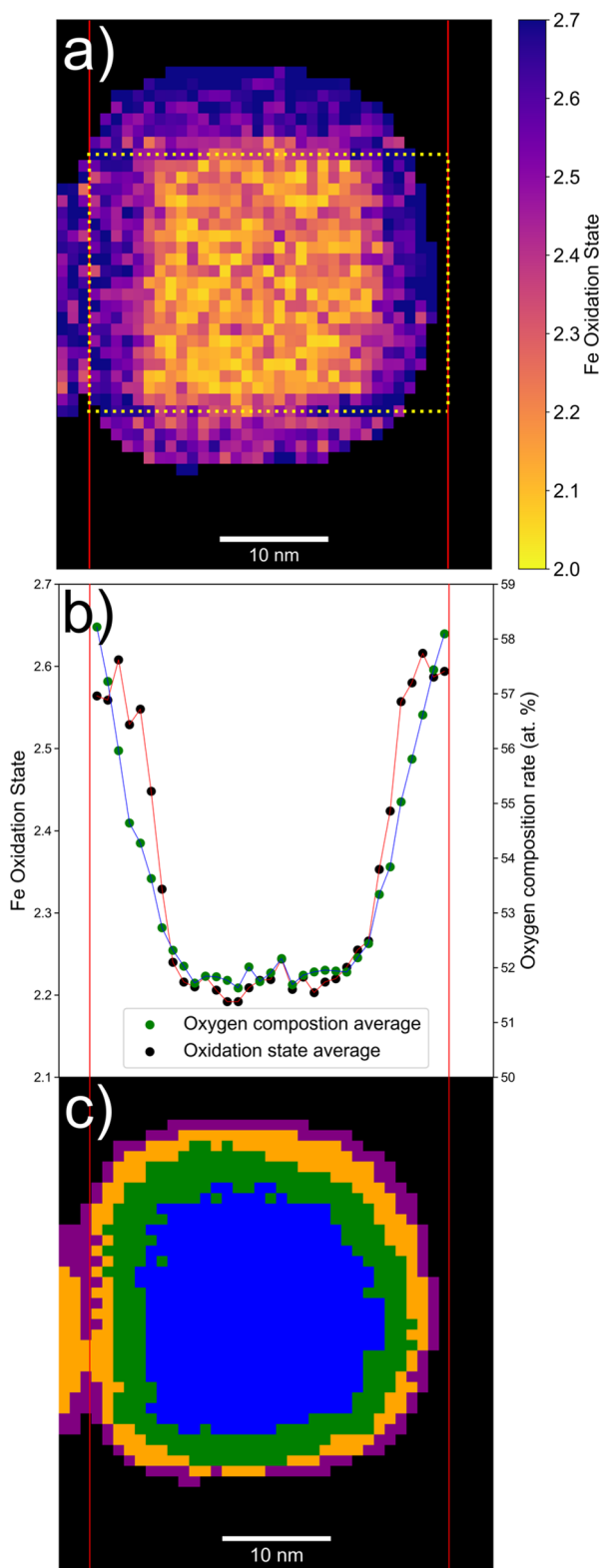


Figure 2. (a) Color map of the iron oxidation states of a FeO/Fe₃O₄ core/shell nanocube obtained from the distance between the oxygen K edge and the L₃ iron white line (method ii, see Methods in Supporting Information). (b) Line profiles of the averaged oxidation state (black dots) and the oxygen elemental composition (green dots; see Figure S3d) (in both cases averaged vertically within the dotted box in (a), and in the first case for the four analysis methods; see Figure S3). (c) Color map with the results of the clustering analysis.

electrons must go through the whole particle (core and both upper and lower shells), the shells also contribute to the EELS signal represented in the core regions.

An elemental quantification was also extracted from the EELS data. The results are shown in the color map of Figure S3d, where it is presented the oxygen elemental composition in atomic percent (atom %). This map also shows the core/shell structure, exhibiting an oxygen composition of about 57 atom % for the shell regions (in agreement to the magnetite stoichiometry), and an oxygen composition of around 52 atom % for the core region, which is a slightly higher than the expected stoichiometry for wüstite (50 atom %) but consistent with having the upper and lower magnetite shells. The oxygen concentration profile presented in Figure 2b (right axis) has been also calculated by averaging the corresponding values inside the dotted box in Figure 2a.

The results of these averaged quantifications (oxidation state and oxygen composition) definitely confirm the presence of an oxidation gradient near the core/shell interface extending about 3.0 ± 0.5 nm from the interface (as depicted in Figure 2b). In addition, there is an almost perfect agreement between the oxidation gradient and the composition gradient. Thus, the sample could be better described as FeO/Fe_xO_y/Fe₃O₄. Note that although the presence of such a graded interface had already been proposed for FeO/Fe₃O₄ nanoparticles using diverse approaches (lattice parameter examination, X-ray analysis, and Mössbauer analysis).^{13,48–50} The EELS oxidation and compositional maps give a definitive proof of the origin of the gradient, which is mainly related to the change of the oxidation state.

To further confirm the graded interface in the FeO/Fe₃O₄ nanocubes, we used principal component analysis (PCA)⁵¹ (to reduce the noise) and k-means clustering algorithm³² (to identify different zones in the nanoparticle) (see Methods in Supporting Information). This latter technique allows detecting areas in the nanoparticle with analogous EELS characteristics. Interestingly, the clustering algorithm identifies four concentric areas of distinct properties, that is, inner core/outer core/inner shell/outer shell (Figure 2c). When comparing these clusters with the averaged oxidation state, the second and third clusters coincide with the oxidation and compositional gradients (Figure 2). Thus, the interface region (where the gradients are found) is identified by the clustering algorithm as two clusters, which is independently verified by the elemental quantification and oxidation state analysis. Consequently, the gradient zone is composed of two dissimilar regions, which can be interpreted as the nanoparticle being formed by a multishell, “onionlike”, structure, FeO/Fe_{1+x}O/Fe_{3–δ}O₄/Fe₃O₄, as proposed by Ichikawa et al.¹³

Finally, note that the pure Fe₃O₄ nanoparticles exhibit a very homogeneous oxidation state ($+2.65 \pm 0.05$; using the four analysis approaches) as well as a homogeneous oxygen composition over the whole particle (Figure S1d,e), corroborating that the graded oxidation interphase in the bimagnetic system is an intrinsic configuration at the core–shell interface rather than to a spurious self-reduction/oxidation process of the Fe₃O₄ phase or the surrounding medium.^{52,53}

Electron Magnetic Circular Dichroism (EMCD). In order to investigate the effect of the graded interface on the magnetic structure of the FeO/Fe₃O₄ nanocubes, we carried out an EMCD study at low temperature. Two EEL spectra with different chirality were obtained in two-beam conditions for each nanocube (see Methods in Supporting Information).

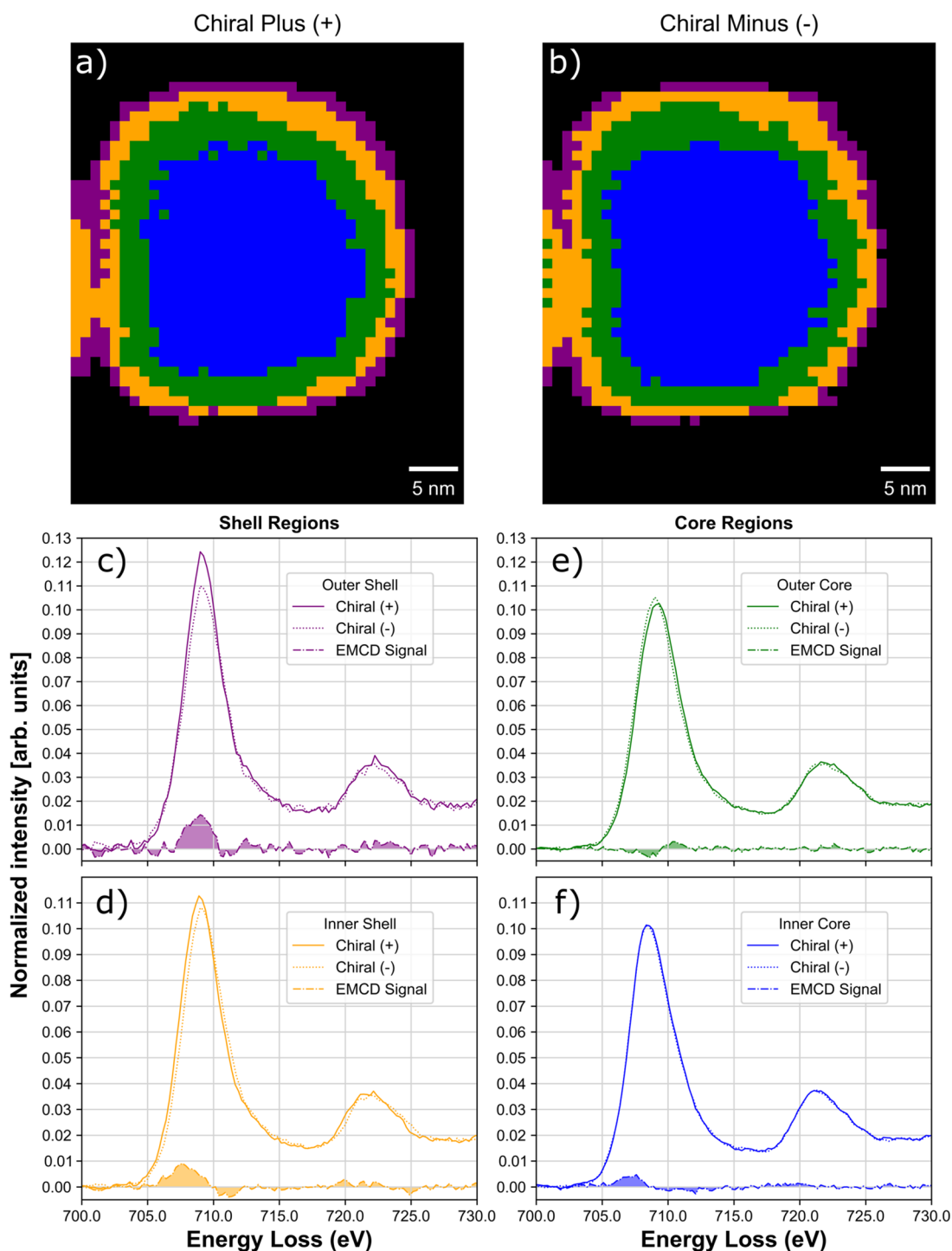


Figure 3. Color maps resulting from the clustering analysis for (a) chiral (+) and (b) chiral (–) configuration of a core/shell nanocube. (c–f) Spectra of the + and – chiralities for each section identified in the clustering and the corresponding EMCD signal: (c) outer shell (violet); (d) inner shell (orange); (e) outer core (green); and (f) inner core (blue).

206 The spectra correspond to the “chiral +” (right circular
 207 polarization) and the “chiral –” (left circular polarization),
 208 respectively. The + and – spectra were subject to the same
 209 previous corrections and clustering algorithms (see Methods in
 210 Supporting Information).

211 First, we analyzed several pure Fe_3O_4 nanocubes to serve as
 212 reference. The clustering analysis of the + and – spectra
 213 revealed homogeneous EEL spectra over the whole sample.
 214 Figure S4 shows the EEL spectra corresponding to the two

different chiralities. The spectra are clearly different (Figure
 S4). Subtracting the + from the – spectra, we obtain the
 EMCD signal corresponding to the Fe_3O_4 nanocubes (Figure
 S4). The EMCD results obtained for the different particles are
 quite similar and comparable to literature data on Fe_3O_4 films
 and nanoparticles.^{29–31}

Next, we analyzed the + and – EEL spectra for the core/
 shell nanocubes. Importantly, since a pixel-by-pixel comparison
 would be extremely complex in our case due to the weak and

224 noisy signal and the small thermal drifts during the acquisition
 225 of the two different chiralities (resulting from small temper-
 226 ature fluctuations), we used the clustering algorithm to identify
 227 equivalent regions for each chirality. Note that the clustering
 228 procedure allows in a simple and efficient way, to classify the
 229 large quantity of spectra from the nanocubes and to reduce the
 230 intrinsic noise in data by averaging all of the spectra within a
 231 given cluster. As expected, the clustering results (i.e., areas with
 232 analogous characteristics) were very similar for both chiralities
 233 (Figure 3a,b). Similar to the pure Fe_3O_4 nanocubes, when
 234 comparing the EEL spectra of equivalent clusters in the two
 235 chiralities it can be clearly seen that the \pm EEL spectra are
 236 slightly different (Figure 3c–f). By subtracting the + and –
 237 spectra for the equivalent regions, we obtain the EMCD
 238 spectra of that given area (see Figure 3c–f).^{54,55} Remarkably,
 239 the EMCD spectra for all of the four regions are distinctly
 240 different. This implies that the oxidation gradient induces
 241 unambiguous changes in the magnetic structure of the
 242 nanocubes. Notably, although the intensity decreases the
 243 shape of the spectra for the four regions is somewhat similar
 244 (and similar to the Fe_3O_4 reference sample). This is somewhat
 245 expected for the surface and inner shell since they are both
 246 mainly Fe_3O_4 . However, the outer and inner regions of the
 247 core are mostly FeO, thus some changes in the EMCD spectra
 248 could potentially be anticipated. The inner FeO core should be
 249 antiferromagnetic at 100 K (Néel temperature $T_N \sim 200$ K;
 250 Figure S5),³⁷ thus no circular dichroism would be expected.
 251 Hence, the dichroic signal should arise mainly from the
 252 contribution of the Fe_3O_4 shells (since the electrons have to go
 253 through the shell before and after they probe the core).
 254 Concerning the Fe_{1+x}O outer core, it is well-known that the
 255 vacancies in Fe_{1+x}O tend to cluster, forming Fe_3O_4 -like regions
 256 inside an FeO matrix.⁵⁶ Consequently, it is not surprising that
 257 the EMCD spectrum of the Fe_{1+x}O outer core is similar to the
 258 shell signals.

259 To get further insight into the magnetic structure, we tried
 260 to quantify the dichroic signal of the different regions.
 261 Unfortunately, the measuring conditions do not allow to
 262 obtain the absolute magnetic moment for each region.⁵⁷
 263 However, since all of the measurements were carried out in the
 264 same conditions, relative magnetic moments can be obtained
 265 by integrating the area of the EMCD peaks and compared
 266 among them. As can be seen in Figure 4, a clear trend emerges
 267 from the relative moments. The outer shell has the largest
 268 magnetic moment, which decreases toward the inner shell
 269 becoming the smallest in the two core regions (Figure 4),
 270 evidencing that the oxidation gradient induces a magnetic
 271 gradient in the nanoparticles. However, two unusual features
 272 can be identified. First, the magnetic moment of the shell
 273 seems to be larger than the reference pure Fe_3O_4 nanocubes.
 274 This is somewhat unexpected since in pure Fe_3O_4 nano-
 275 particles the surface tends to have a lower magnetic moment
 276 than the bulk due to surface disorder.²⁹ Nevertheless, it is
 277 important to emphasize that magnetic moments considerably
 278 larger than bulk values have been often reported in Fe_3O_4 (and
 279 other ferrites) thin films.^{58–61} These enhanced moments are
 280 typically reported to occur for very thin films or at surfaces and
 281 are usually linked to specific defects such as grain boundaries,
 282 vacancies, or antiphase boundaries.^{58–61} Thus, common
 283 defects often observed in this type of (and similar) nano-
 284 particles, such as cation inversion, lattice distortions, Fe^{2+}
 285 vacancies, or grain boundaries could also contribute to the
 286 enhanced moment.^{37,49,62,63} The second possible uncommon

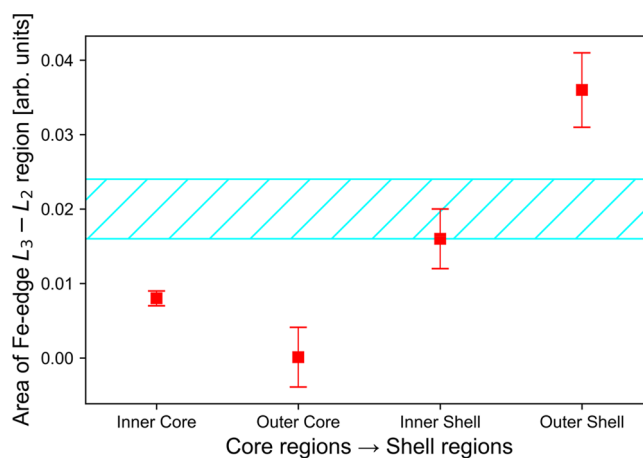


Figure 4. Area of the EMCD spectra for the different clusters. The blue region depicts the area calculated for the pure Fe_3O_4 nanocubes (see Figure S4) where the width of the band corresponds to the standard deviation of the results for the different particles.

effect that can be inferred for the magnetic moment is the
 287 unusually low moment in the outer Fe_{1+x}O core. Namely, due
 288 to vacancy clustering Fe_{1+x}O is expected to have larger
 289 moment than FeO. In contrast, the moment of the Fe_{1+x}O
 290 region seems to be slightly smaller than the one in the FeO
 291 region. This implies that the intrinsic moment of the Fe_{1+x}O
 292 outer core should be opposite to the concomitant contribution
 293 of the $\text{Fe}_{3-\delta}\text{O}_4/\text{Fe}_3\text{O}_4$ shells (arising from the path of the
 294 electrons). The simplest way to account for this effect is
 295 probably to assume an antiferromagnetic coupling between the
 296 Fe_3O_4 shell and the vacancy-induced ferrimagnetic-like spins of
 297 the core (as predicted theoretically and hinted experimentally
 298 for FeO/ Fe_3O_4 and actually observed for other FeO-based
 299 systems^{63–65}). In fact, this assumption could be supported by
 300 the unusually large downturn in $M(T)$ below T_N of FeO
 301 (Figure S5). Note that antiferromagnetic core/shell interface
 302 coupling has actually been reported in other iron oxide-based
 303 bimagnetic core/shell nanoparticles.^{17,66}

In addition, the overall results of the same type of analysis
 305 applied to other particles (by studying a section of the
 306 nanoparticle rather than the whole nanoparticle) were
 307 comparable, confirming the presence of a gradual change of
 308 the oxidation state at the interface leading to a magnetic
 309 gradient (see Supporting Information; Figure S6).

Notably, this STEM-based EELS approach merging
 311 compositional and magnetic information is not only limited
 312 to oxide-based core/shell nanoparticles, but it could also be
 313 applied to other types of core/shell structures (e.g., metal/
 314 metal, metal/oxide) and to other morphologies (e.g., Janus
 315 nanoparticles) or even inhomogeneous nanoparticles (e.g.,
 316 phase segregation) or nanostructured composites.

CONCLUSIONS

In summary, we have demonstrated that the combination of
 319 EELS compositional mapping and EMCD is an excellent
 320 option to unravel the correlation between the structural/
 321 morphological and magnetic structure in bimagnetic core/shell
 322 nanoparticles. Importantly, by using a clustering algorithm the
 323 analysis of the EMCD can be greatly simplified but still achieve
 324 nanometer resolution. The results show that the $\text{FeO}/\text{Fe}_3\text{O}_4$
 325 nanocubes have an interdiffused interface leading to a $\text{FeO}/$
 326 $\text{Fe}_{1+x}\text{O}/\text{Fe}_{3-\delta}\text{O}_4/\text{Fe}_3\text{O}_4$ onionlike structure. This structure

328 results in a graded magnetic configuration with some unusual
329 features, like an enhanced moment for the surface Fe₃O₄ shell.
330 These results open new avenues for studying the magnetic
331 properties of not only complex magnetic nanoparticles but also
332 nanostructured materials.

333 ■ ASSOCIATED CONTENT


334 **SI** Supporting Information


335 The Supporting Information is available free of charge at
336 <https://pubs.acs.org/doi/10.1021/acs.nanolett.1c02089>.

337 Descriptions and details of the experimental methods:
338 nanoparticles synthesis, morphological characterization,
339 electron energy-loss spectroscopy, determination of
340 oxidation state, determination of the elemental composi-
341 tion, the electron magnetic circular dichroism technique,
342 and magnetic characterization; Figures S1 to S9 (PDF)


343 ■ AUTHOR INFORMATION

344 Corresponding Authors

345 **Daniel del-Pozo-Bueno** – *LENS-MIND, Department*
346 *Enginyeries Electrònica i Biomèdica, Universitat de Barcelona,*
347 *E-08028 Barcelona, Spain; Institute of Nanoscience and*
348 *Nanotechnology of the University of Barcelona (IN2UB), E-*
349 *08028 Barcelona, Spain;  [orcid.org/0000-0003-1819-](https://orcid.org/0000-0003-1819-298X)*
350 *298X; Email: ddelpozo@ub.edu*


351 **María Varela** – *Departamento de Física de Materiales e*
352 *Instituto Pluridisciplinar, Universidad Complutense de*
353 *Madrid (UCM), 28040 Madrid, Spain;  [orcid.org/0000-](https://orcid.org/0000-0002-6582-7004)*
354 *0002-6582-7004; Email: mvarela@ucm.es*

355 **Alberto López-Ortega** – *Departamento de Ciencias,*
356 *Universidad Pública de Navarra, 31006 Pamplona, Spain;*
357 *Institute for Advanced Materials and Mathematics INAMAT,*
358 *Universidad Pública de Navarra, 31006 Pamplona, Spain;*
359 * orcid.org/0000-0003-3440-4444;*
360 *Email: lopezortega.alberto@gmail.com*

361 **Alejandro G. Roca** – *Catalan Institute of Nanoscience and*
362 *Nanotechnology (ICN2), CSIC and BIST, 08193 Barcelona,*
363 *Spain;  orcid.org/0000-0001-6610-9197;*
364 *Email: alejandrogomez@icn2.cat*

365 Authors

366 **Marta Estrader** – *Departament de Química Inorgànica i*
367 *Orgànica, Universitat de Barcelona, E-08028 Barcelona,*
368 *Spain; Institute of Nanoscience and Nanotechnology of the*
369 *University of Barcelona (IN2UB), E-08028 Barcelona, Spain*

370 **Josep Nogués** – *Catalan Institute of Nanoscience and*
371 *Nanotechnology (ICN2), CSIC and BIST, 08193 Barcelona,*
372 *Spain; ICREA, E-08010 Barcelona, Spain;  [orcid.org/](https://orcid.org/0000-0003-4616-1371)*
373 *0000-0003-4616-1371*

374 **Francesca Peiró** – *LENS-MIND, Department Enginyeries*
375 *Electrònica i Biomèdica, Universitat de Barcelona, E-08028*
376 *Barcelona, Spain; Institute of Nanoscience and*
377 *Nanotechnology of the University of Barcelona (IN2UB), E-*
378 *08028 Barcelona, Spain*

379 **Sònia Estradé** – *LENS-MIND, Department Enginyeries*
380 *Electrònica i Biomèdica, Universitat de Barcelona, E-08028*
381 *Barcelona, Spain; Institute of Nanoscience and*
382 *Nanotechnology of the University of Barcelona (IN2UB), E-*
383 *08028 Barcelona, Spain*

384 Complete contact information is available at:
385 <https://pubs.acs.org/doi/10.1021/acs.nanolett.1c02089>

Notes

The authors declare no competing financial interest.

■ ACKNOWLEDGMENTS

The authors acknowledge the financial support from the Spanish Minister of Science and Innovation (MICINN) through the projects PID2019-106165GB-C21, PID2019-106165GB-C22, and PID2019-106229RB-I00. They also acknowledge funding from Generalitat de Catalunya through the 2017-SGR-292 and 2017-SGR-776 projects. In addition, research at UCM was supported by MINECO/FEDER MAT2015-66888-C3-3-R and RTI2018-097895-B-C43 grants. ICN2 is funded by the CERCA programme/Generalitat de Catalunya. The ICN2 is supported by the Severo Ochoa Centres of Excellence programme, funded by the Spanish Research Agency (AEI, Grant SEV-2017-0706). M.E. thanks the Spanish MICINN and AEI/FSE for Ramón y Cajal contract (RYC2018-024396-I). A.L.O. acknowledges support from the Universidad Pública de Navarra (Grant PJUP-NA2020). STEM-EELS observations carried out at the Centro Nacional de Microscopía Electrónica at Universidad Complutense de Madrid, Spain (ICTS ELECMI).

■ REFERENCES

- (1) Wilks, S. P. Engineering and Investigating the Control of Semiconductor Surfaces and Interfaces. *J. Phys. D: Appl. Phys.* **2002**, *35*, R77–R90.
- (2) Jang, Y.; Shapiro, A.; Isarov, M.; Rubin-Brusilovski, A.; Safran, A.; Budniak, A. K.; Horani, F.; Dehnel, J.; Sashchiuk, A.; Lifshitz, E. Interface Control of Electronic and Optical Properties in IV-VI and II-VI Core/Shell Colloidal Quantum Dots: A Review. *Chem. Commun.* **2017**, *53*, 1002–1024.
- (3) Xu, J.; Zhu, K.; Hou, Y. Magnetic Heterostructures: Interface Control to Optimize Magnetic Property and Multifunctionality. *ACS Appl. Mater. Interfaces* **2020**, *12*, 36811–36822.
- (4) Hellman, F.; Hoffmann, A.; Tserkovnyak, Y.; Beach, G. S. D.; Fullerton, E. E.; Leighton, C.; MacDonald, A. H.; Ralph, D. C.; Arena, D. A.; Durr, H. A.; Fischer, P.; Grollier, J.; Heremans, J. P.; Jungwirth, T.; Kimel, A. V.; Koopmans, B.; Krivorotov, I. N.; May, S. J.; Petford-Long, A. K.; Rondinelli, J. M.; Samarth, N.; Schuller, I. K.; Slavin, A. N.; Stiles, M. D.; Tchernyshyov, O.; Thiaville, A.; Zink, B. L. Interface-Induced Phenomena in Magnetism. *Rev. Mod. Phys.* **2017**, *89*, 025006.
- (5) Zubko, P.; Gariglio, S.; Gabay, M.; Ghosez, P.; Triscone, J. M. Interface Physics in Complex Oxide Heterostructures. *Annu. Rev. Condens. Matter Phys.* **2011**, *2*, 141–165.
- (6) Huang, Z.; Ariando; Renshaw Wang, X.; Rusydi, A.; Chen, J.; Yang, H.; Venkatesan, T. Interface Engineering and Emergent Phenomena in Oxide Heterostructures. *Adv. Mater.* **2018**, *30*, 1802439.
- (7) Laureti, S.; Gerardino, A.; D’Acapito, F.; Peddis, D.; Varvaro, G. The Role of Chemical and Microstructural Inhomogeneities on Interface Magnetism. *Nanotechnology* **2021**, *32*, 205701.
- (8) Fallarino, L.; Kirby, B.; Fullerton, E. Graded Magnetic Materials. *J. Phys. D: Appl. Phys.* **2021**, *54*, 303002.
- (9) Chen, Y.; Jiang, H.; Li, L.; Wang, Q.; Du, L.; Liu, X.; Tian, G. Hierarchical NiS Decorated CuO@ZnFe₂O₄ Nanoarrays as Advanced Photocathodes for Hydrogen Evolution Reaction. *Int. J. Hydrogen Energy* **2020**, *45*, 6174–6183.
- (10) Hu, L.; Brüner, P.; Grehl, T.; Brongersma, H. H.; Cabana, J. Control of Chemical Structure in Core-Shell Nanocrystals for the Stabilization of Battery Electrode/Electrolyte Interfaces. *Chem. Mater.* **2017**, *29*, 5896–5905.
- (11) Boldt, K.; Bartlett, S.; Kirkwood, N.; Johannessen, B. Quantification of Material Gradients in Core/Shell Nanocrystals Using EXAFS Spectroscopy. *Nano Lett.* **2020**, *20*, 1009–1017.

- 450 (12) López-Ortega, A.; Estrader, M.; Salazar-Alvarez, G.; Estradé, S.;
451 Golosovsky, I. V.; Dumas, R. K.; Keavney, D. J.; Vasilakaki, M.;
452 Trohidou, K. N.; Sort, J.; Peiró, F.; Suriñach, S.; Baró, M. D.; Nogués,
453 J. Strongly Exchange Coupled Inverse Ferrimagnetic Soft/Hard,
454 $\text{Mn}_x\text{Fe}_{3-x}\text{O}_4/\text{Fe}_x\text{Mn}_{3-x}\text{O}_4$ Core/Shell Heterostructured Nanoparticles.
455 *Nanoscale* **2012**, *4*, 5138–5147.
- 456 (13) Ichikawa, R. U.; Roca, A. G.; López-Ortega, A.; Estrader, M.;
457 Peral, I.; Turrillas, X.; Nogués, J. Combining X-Ray Whole Powder
458 Pattern Modeling, Rietveld and Pair Distribution Function Analyses
459 as a Novel Bulk Approach to Study Interfaces in Heteronanopar-
460 ticles: Oxidation Front in $\text{FeO}/\text{Fe}_3\text{O}_4$ Core/Shell Nanoparticles
461 as a Case Study. *Small* **2018**, *14*, 1800804.
- 462 (14) Muro-Cruces, J.; Roca, A. G.; López-Ortega, A.; Fantechi, E.;
463 Del-Pozo-Bueno, D.; Estradé, S.; Peiró, F.; Sepúlveda, B.; Pineiro, F.;
464 Sangregorio, C.; Nogués, J. Precise Size Control of the Growth of
465 Fe_3O_4 Nanocubes over a Wide Size Range Using a Rationally
466 Designed One-Pot Synthesis. *ACS Nano* **2019**, *13*, 7716–7728.
- 467 (15) Krycka, K. L.; Borchers, J. A.; Salazar-Alvarez, G.; López-
468 Ortega, A.; Estrader, M.; Estradé, S.; Winkler, E.; Zysler, R. D.; Sort,
469 J.; Peiró, F.; Baró, M. D.; Kao, C. C.; Nogués, J. Resolving Material-
470 Specific Structures within $\text{Fe}_3\text{O}_4/\gamma\text{-Mn}_2\text{O}_3$ Core/Shell Nanoparticles
471 Using Anomalous Small-Angle X-Ray Scattering. *ACS Nano* **2013**, *7*,
472 921–931.
- 473 (16) Winkler, E. L.; Zysler, R. D. Core/Shell Bimagnetic
474 Nanoparticles. In *New Trends in Nanoparticle Magnetism*; Springer
475 International Publishing: Cham, Switzerland, 2021; pp 87–106.
- 476 (17) Estrader, M.; López-Ortega, A.; Estradé, S.; Golosovsky, I. V.;
477 Salazar-Alvarez, G.; Vasilakaki, M.; Trohidou, K. N.; Varela, M.;
478 Stanley, D. C.; Sinko, M.; Pechan, M. J.; Keavney, D. J.; Peiró, F.;
479 Suriñach, S.; Baró, M. D.; Nogués, J. Robust Antiferromagnetic
480 Coupling in Hard-Soft Bi-Magnetic Core/Shell Nanoparticles. *Nat.*
481 *Commun.* **2013**, *4*, 2960.
- 482 (18) Lavorato, G. C.; Das, R.; Alonso Masa, J.; Phan, M.-H.;
483 Srikanth, H. Hybrid Magnetic Nanoparticles as Efficient Nanoheaters
484 in Biomedical Applications. *Nanoscale Adv.* **2021**, *3*, 867–888.
- 485 (19) De Toro, J. A.; Marques, D. P.; Muñiz, P.; Skumryev, V.; Sort,
486 J.; Givord, D.; Nogués, J. High Temperature Magnetic Stabilization of
487 Cobalt Nanoparticles by an Antiferromagnetic Proximity Effect. *Phys.*
488 *Rev. Lett.* **2015**, *115*, 57201.
- 489 (20) López-Ortega, A.; Estrader, M.; Salazar-Alvarez, G.; Roca, A.
490 G.; Nogués, J. Applications of Exchange Coupled Bi-Magnetic Hard/
491 Soft and Soft/Hard Magnetic Core/Shell Nanoparticles. *Phys. Rep.*
492 **2015**, *553*, 1–32.
- 493 (21) Kamzin, A. S.; Obaidat, I. M.; Valliulin, A. A.; Semenov, V. G.;
494 Al-Omari, I. A. The Composition and Magnetic Structure of $\text{Fe}_3\text{O}_4/\gamma$ -
495 Fe_2O_3 Core-Shell Nanocomposites at 300 and 80 K: Mössbauer
496 Study (Part I). *Phys. Solid State* **2020**, *62*, 1933–1943.
- 497 (22) Juhin, A.; López-Ortega, A.; Sikora, M.; Carvallo, C.; Estrader,
498 M.; Estradé, S.; Peiró, F.; Baró, M. D.; Sainctavit, P.; Glatzel, P.;
499 Nogués, J. Direct Evidence for an Interdiffused Intermediate Layer in
500 Bi-magnetic Core-Shell Nanoparticles. *Nanoscale* **2014**, *6*, 11911–
501 11920.
- 502 (23) Oberdick, S. D.; Abdelgawad, A.; Moya, C.; Mesbahi-Vasey, S.;
503 Kepaptsoglou, D.; Lazarov, V. K.; Evans, R. F. L.; Meilak, D.;
504 Skoropata, E.; Van Lierop, J.; Hunt-Isaak, I.; Pan, H.; Jiri, Y.; Krycka,
505 K. L.; Borchers, J. A.; Majetich, S. A. Spin Canting across Core/Shell
506 $\text{Fe}_3\text{O}_4/\text{Mn}_x\text{Fe}_{3-x}\text{O}_4$ Nanoparticles. *Sci. Rep.* **2018**, *8*, 3425.
- 507 (24) Krycka, K. L.; Borchers, J. A.; Laver, M.; Salazar-Alvarez, G.;
508 López-Ortega, A.; Estrader, M.; Suriñach, S.; Baró, M. D.; Sort, J.;
509 Nogués, J. Correlating Material-Specific Layers and Magnetic
510 Distributions within Onion-like $\text{Fe}_3\text{O}_4/\text{MnO}/\gamma\text{-Mn}_2\text{O}_3$ Core/Shell
511 Nanoparticles. *J. Appl. Phys.* **2013**, *113*, 17B531.
- 512 (25) Pichon, B. P.; Gerber, O.; Lefevre, C.; Florea, I.; Fleutot, S.;
513 Baaziz, W.; Pauly, M.; Ohlmann, M.; Ulhaq, C.; Ersen, O.; Pierron-
514 Bohnes, V.; Panissod, P.; Drillon, M.; Begin-Colin, S. Microstructural
515 and Magnetic Investigations of Wüstite-Spinel Core-Shell Cubic-
516 Shaped Nanoparticles. *Chem. Mater.* **2011**, *23*, 2886–2900.
- 517 (26) Yang, M.-D.; Ho, C.-H.; Ruta, S.; Chantrell, R.; Krycka, K.;
518 Hovorka, O.; Chen, F.-R.; Lai, P.-S.; Lai, C.-H. Magnetic Interaction
of Multifunctional Core-Shell Nanoparticles for Highly Effective
519 Theranostics. *Adv. Mater.* **2018**, *30*, 1802444. 520
- (27) Rubino, S.; Schattschneider, P.; Stöger-Pollach, M.; Hébert, C.;
521 Ruzs, J.; Calmels, L.; Warot-Fonrose, B.; Houdellier, F.; Serin, V.;
522 Novak, P. Energy-Loss Magnetic Chiral Dichroism (EMCD):
523 Magnetic Chiral Dichroism in the Electron Microscope. *J. Mater.*
524 *Res.* **2008**, *23*, 2582–2590. 525
- (28) Schattschneider, P.; Stöger-pollach, M.; Rubino, S.; Sperl, M.;
526 Hurm, C.; Zweck, J.; Ruzs, J. Detection of Magnetic Circular
527 Dichroism on the Two-Nanometer Scale. *Phys. Rev. B: Condens.*
528 *Matter Mater. Phys.* **2008**, *78*, 104413. 529
- (29) Salafranca, J.; Gazquez, J.; Pérez, N.; Labarta, A.; Pantelides, S.
530 T.; Pennycook, S. J.; Batlle, X.; Varela, M. Surfactant Organic
531 Molecules Restore Magnetism in Metal-Oxide Nanoparticle Surfaces.
532 *Nano Lett.* **2012**, *12*, 2499–2503. 533
- (30) Thersleff, T.; Ruzs, J.; Rubino, S.; Hjörvarsson, B.; Ito, Y.;
534 Zaluzec, N.; Leifer, K. Quantitative Analysis of Magnetic Spin and
535 Orbital Moments from an Oxidized Iron (1 1 0) Surface Using
536 Electron Magnetic Circular Dichroism. *Sci. Rep.* **2015**, *5*, 13012. 537
- (31) Stöger-Pollach, M.; Treiber, C. D.; Resch, G. P.; Keays, D. A.;
538 Ennen, I. EMCD Real Space Maps of Magnetospirillum Magneto-
539 tacticum. *Micron* **2011**, *42*, 456–460. 540
- (32) Torruella, P.; Estrader, M.; López-Ortega, A.; Baró, M. D.;
541 Varela, M.; Peiró, F.; Estradé, S. Clustering Analysis Strategies for
542 Electron Energy Loss Spectroscopy (EELS). *Ultramicroscopy* **2018**,
543 *185*, 42–48. 544
- (33) Lak, A.; Cassani, M.; Mai, B. T.; Winkelmann, N.; Cabrera, D.;
545 Sadrollahi, E.; Marras, S.; Remmer, H.; Fiorito, S.; Cremades-Jimeno,
546 L.; Litterst, F. J.; Ludwig, F.; Manna, L.; Teran, F. J.; Bals, S.;
547 Pellegrino, T. Fe^{2+} Deficiencies, FeO Subdomains, and Structural
548 Defects Favor Magnetic Hyperthermia Performance of Iron Oxide
549 Nanocubes into Intracellular Environment. *Nano Lett.* **2018**, *18*,
550 6856–6866. 551
- (34) Khurshid, H.; Alonso, J.; Nemati, Z.; Phan, M. H.; Mukherjee,
552 P.; Fdez-Gubieda, M. L.; Barandiarán, J. M.; Srikanth, H. Anisotropy
553 Effects in Magnetic Hyperthermia: A Comparison between Spherical
554 and Cubic Exchange-Coupled $\text{FeO}/\text{Fe}_3\text{O}_4$ Nanoparticles. *J. Appl.*
555 *Phys.* **2015**, *117*, 17A337. 556
- (35) Zheng, J.; Yu, Z.; Ji, G.; Lin, X.; Lv, H.; Du, Y. Reduction
557 Synthesis of $\text{Fe}_x\text{O}_y@\text{SiO}_2$ Core-Shell Nanostructure with Enhanced
558 Microwave-Absorption Properties. *J. Alloys Compd.* **2014**, *602*, 8–15. 559
- (36) Lak, A.; Dieckhoff, J.; Ludwig, F.; Scholtyssek, J. M.;
560 Goldmann, O.; Lünsdorf, H.; Eberbeck, D.; Kornowski, A.; Kraken,
561 M.; Litterst, F. J.; Fiege, K.; Mischnick, P.; Schilling, M. Highly Stable
562 Monodisperse PEGylated Iron Oxide Nanoparticle Aqueous
563 Suspensions: A Nontoxic Tracer for Homogeneous Magnetic
564 Bioassays. *Nanoscale* **2013**, *5*, 11447–11455. 565
- (37) Estrader, M.; López-Ortega, A.; Golosovsky, I. V.; Estradé, S.;
566 Roca, A. G.; Salazar-Alvarez, G.; López-Conesa, L.; Tobia, D.;
567 Winkler, E.; Ardisson, J. D.; Macedo, W. A. A.; Morphis, A.;
568 Vasilakaki, M.; Trohidou, K. N.; Gukasov, A.; Mirebeau, L.; Makarova,
569 O. L.; Zysler, R. D.; Peiró, F.; Baró, M. D.; Bergström, L.; Nogués, J.
570 Origin of the Large Dispersion of Magnetic Properties in Nano-
571 structured Oxides: $\text{Fe}_x\text{O}/\text{Fe}_3\text{O}_4$ Nanoparticles as a Case Study.
572 *Nanoscale* **2015**, *7*, 3002–3015. 573
- (38) Torruella, P.; Arenal, R.; De La Peña, F.; Saghi, Z.; Yedra, L.;
574 Eljarrat, A.; López-Conesa, L.; Estrader, M.; López-Ortega, A.;
575 Salazar-Alvarez, G.; Nogués, J.; Ducati, C.; Midgley, P. A.; Peiró, F.;
576 Estradé, S. 3D Visualization of the Iron Oxidation State in $\text{FeO}/$
577 Fe_3O_4 Core-Shell Nanocubes from Electron Energy Loss Tomog-
578 raphy. *Nano Lett.* **2016**, *16*, 5068–5073. 579
- (39) Roldan, M. A.; Mayence, A.; López-Ortega, A.; Ishikawa, R.;
580 Salafranca, J.; Estrader, M.; Salazar-Alvarez, G.; Dolores Baró, M.;
581 Nogués, J.; Pennycook, S. J.; Varela, M. Probing the Meta-Stability of
582 Oxide Core/Shell Nanoparticle Systems at Atomic Resolution. *Chem.*
583 *Eng. J.* **2021**, *405*, 126820. 584
- (40) Colliex, C.; Manoubi, T.; Ortiz, C. Electron-Energy-Loss-
585 Spectroscopy near-Edge Fine Structures in the Iron-Oxygen System.
586 *Phys. Rev. B: Condens. Matter Mater. Phys.* **1991**, *44*, 11402–11411. 587

- 588 (41) Varela, M.; Oxley, M. P.; Luo, W.; Tao, J.; Watanabe, M.;
589 Lupini, A. R.; Pantelides, S. T.; Pennycook, S. J. Atomic-Resolution
590 Imaging of Oxidation States in Manganites. *Phys. Rev. B: Condens.*
591 *Matter Mater. Phys.* **2009**, *79*, 085117.
- 592 (42) Tan, H.; Verbeeck, J.; Abakumov, A.; van Tendeloo, G.
593 Oxidation State and Chemical Shift Investigation in Transition Metal
594 Oxides by EELS. *Ultramicroscopy* **2012**, *116*, 24–33.
- 595 (43) Yedra, L.; Xuriguera, E.; Estrader, M.; López-Ortega, A.; Baró,
596 M. D.; Nogués, J.; Roldan, M.; Varela, M.; Estradé, S.; Peiró, F. Oxide
597 Wizard: An EELS Application to Characterize the White Lines of
598 Transition Metal Edges. *Microsc. Microanal.* **2014**, *20*, 698–705.
- 599 (44) Arévalo-López, A. M.; Alario-Franco, M. A. Reliable Method
600 for Determining the Oxidation State in Chromium Oxides. *Inorg.*
601 *Chem.* **2009**, *48*, 11843–11846.
- 602 (45) Luo, K.; Roberts, M. R.; Hao, R.; Guerrini, N.; Pickup, D. M.;
603 Liu, Y. S.; Edström, K.; Guo, J.; Chadwick, A. v.; Duda, L. C.; Bruce,
604 P. G. Charge-Compensation in 3d-Transition-Metal-Oxide Intercala-
605 tion Cathodes through the Generation of Localized Electron Holes on
606 Oxygen. *Nat. Chem.* **2016**, *8*, 684–691.
- 607 (46) van Aken, P. A.; Liebscher, B. Quantification of Ferrous/Ferric
608 Ratios in Minerals: New Evaluation Schemes of Fe L₂₃ Electron
609 Energy-Loss near-Edge Spectra. *Phys. Chem. Miner.* **2002**, *29*, 188–
610 200.
- 611 (47) Calvert, C. C.; Brown, A.; Brydson, R. Determination of the
612 Local Chemistry of Iron in Inorganic and Organic Materials. *J.*
613 *Electron Spectrosc. Relat. Phenom.* **2005**, *143*, 173–187.
- 614 (48) Pichon, B. P.; Gerber, O.; Lefevre, C.; Florea, I.; Fleutot, S.;
615 Baaziz, W.; Pauly, M.; Ohlmann, M.; Ulhaq, C.; Ersen, O.; Pierron-
616 Bohnes, V.; Panissod, P.; Drillon, M.; Begin-Colin, S. Microstructural
617 and Magnetic Investigations of Wüstite-Spinel Core-Shell Cubic-
618 Shaped Nanoparticles. *Chem. Mater.* **2011**, *23*, 2886–2900.
- 619 (49) Wetterskog, E.; Tai, C. W.; Grins, J.; Bergström, L.; Salazar-
620 Alvarez, G. Anomalous Magnetic Properties of Nanoparticles Arising
621 from Defect Structures: Topotaxial Oxidation of Fe_{1-x}O/Fe_{3-δ}O₄ Core
622 shell Nanocubes to Single-Phase Particles. *ACS Nano* **2013**, *7*, 7132–
623 7144.
- 624 (50) Castellanos-Rubio, I.; Rodrigo, I.; Munshi, R.; Arriortua, O.;
625 Garitaonandia, J. S.; Martinez-Amesti, A.; Plazaola, F.; Orue, I.; Pralle,
626 A.; Insausti, M. Outstanding Heat Loss via Nano-Octahedra above 20
627 nm in Size: From Wüstite-Rich Nanoparticles to Magnetite Single-
628 Crystals. *Nanoscale* **2019**, *11*, 16635–16649.
- 629 (51) Cueva, P.; Hovden, R.; Mundy, J. A.; Xin, H. L.; Muller, D. A.
630 Data Processing for Atomic Resolution Electron Energy Loss
631 Spectroscopy. *Microsc. Microanal.* **2012**, *18*, 667–675.
- 632 (52) López-Ortega, A.; Roca, A. G.; Torruella, P.; Petrecca, M.;
633 Estradé, S.; Peiró, F.; Puentes, V.; Nogués, J. Galvanic Replacement
634 onto Complex Metal-Oxide Nanoparticles: Impact of Water or Other
635 Oxidizers in the Formation of Either Fully Dense Onion-like or
636 Multicomponent Hollow MnO_x/FeO_x Structures. *Chem. Mater.* **2016**,
637 *28*, 8025–8031.
- 638 (53) García-García, S.; López-Ortega, A.; Zheng, Y.; Nie, Y.; Cho,
639 K.; Chuvilin, A.; Knez, M. Ligand-Induced Reduction Concerted with
640 Coating by Atomic Layer Deposition on the Example of TiO₂-Coated
641 Magnetite Nanoparticles. *Chem. Sci.* **2019**, *10*, 2171–2178.
- 642 (54) Wang, Z. Q.; Zhong, X. Y.; Yu, R.; Cheng, Z. Y.; Zhu, J.
643 Quantitative Experimental Determination of Site-Specific Magnetic
644 Structures by Transmitted Electrons. *Nat. Commun.* **2013**, *4*, 1395.
- 645 (55) Peña, F.; de la Prestat, E.; Fauske, V. T.; Burdet, P.; Furnival,
646 T.; Jokubauskas, P.; Lähnemann, J.; Nord, M.; Ostasevicius, T.;
647 MacArthur, K. E.; Johnstone, D. N.; Sarahan, M.; Taillon, J.; Aarholt,
648 T.; Migunov, V.; Eljarrat, A.; Caron, J.; Poon, T.; Mazzucco, S.;
649 Martineau, B.; Somnath, S.; Slater, T.; Francis, C.; Tappy, N.; Walls,
650 M.; Cautaearts, N.; Winkler, F.; Donval, G. Hyperspy/Hyperspy,
651 Release v1.6.4.; 2021. DOI: 10.5281/ZENODO.5082777.
- 652 (56) Gavarrí, J. R.; Carel, C. The Complex Nonstoichiometry of
653 Wüstite Fe_{1-x}O: Review and Comments. *Prog. Solid State Chem.* **2019**,
654 *53*, 27–49.
- (57) Rusz, J.; Oppeneer, P. M.; Lidbaum, H.; Rubino, S.; Leifer, K. 655
Asymmetry of the Two-Beam Geometry in EMCD Experiments. *J.* 656
Microsc. **2010**, *237*, 465–468. 657
- (58) Pohlmann, T.; Kuschel, T.; Rodewald, J.; Thien, J.; Ruwisch, 658
K.; Bertram, F.; Weschke, E.; Shafer, P.; Wollschläger, J.; Küpper, K. 659
Cation- And Lattice-Site-Selective Magnetic Depth Profiles of 660
Ulthrin Fe₃O₄ (0 0 1) Films. *Phys. Rev. B: Condens. Matter Mater.* 661
Phys. **2020**, *102*, 220411. 662
- (59) Phase, D. M.; Panchal, G.; Rawat, R.; Tiwari, S.; Prakash, R.; 663
Jain, D.; Choudhary, R. J. Anomalous Magnetic Properties of Fe₃O₄ 664
Nanostructures on GaAs Substrate Probed Using X-Ray Magnetic 665
Circular Dichroism. *J. Magn. Magn. Mater.* **2019**, *482*, 296–300. 666
- (60) Guan, X.; Zhou, G.; Xue, W.; Quan, Z.; Xu, X. The 667
Investigation of Giant Magnetic Moment in Ultrathin Fe₃O₄ Films. 668
APL Mater. **2016**, *4*, 036104. 669
- (61) Herng, T. S.; Xiao, W.; Poh, S. M.; He, F.; Sutarto, R.; Zhu, X.; 670
Li, R.; Yin, X.; Diao, C.; Yang, Y.; Huang, X.; Yu, X.; Feng, Y. P.; 671
Rusydi, A.; Ding, J. Achieving a High Magnetization in Sub- 672
Nanostructured Magnetite Films by Spin-Flipping of Tetrahedral 673
Fe³⁺ Cations. *Nano Res.* **2015**, *8*, 2935–2945. 674
- (62) Torruella, P.; Ruiz-Caridad, A.; Walls, M.; Roca, A. G.; López- 675
Ortega, A.; Blanco-Portals, J.; López-Conesa, L.; Nogués, J.; Peiró, F.; 676
Estradé, S. Atomic-Scale Determination of Cation Inversion in Spinel- 677
Based Oxide Nanoparticles. *Nano Lett.* **2018**, *18*, 5854–5861. 678
- (63) Lappas, A.; Antonaropoulos, G.; Brintakis, K.; Vasilakaki, M.; 679
Trohidou, K. N.; Iannotti, V.; Ausanio, G.; Kostopoulou, A.; 680
Abeykoon, M.; Robinson, I. K.; Bozin, E. S. Vacancy-Driven 681
Noncubic Local Structure and Magnetic Anisotropy Tailoring in 682
Fe_xO-Fe_{3-δ}O₄ Nanocrystals. *Phys. Rev. X* **2019**, *9*, 041044. 683
- (64) Novotny, Z.; Mulakaluri, N.; Edes, Z.; Schmid, M.; Pentcheva, 684
R.; Diebold, U.; Parkinson, G. S. Probing the Surface Phase Diagram 685
of Fe₃O₄ (0 0 1) towards the Fe-Rich Limit: Evidence for Progressive 686
Reduction of the Surface. *Phys. Rev. B: Condens. Matter Mater. Phys.* 687
2013, *87*, 195410. 688
- (65) Wang, B. Y.; Chen, C. J.; Lin, K.; Hsu, C. Y.; Ning, J. Y.; Tsai, 689
M. S.; Chuang, T. H.; Wei, D. H.; Weng, S. C. Promoting Exchange 690
Bias Coupling in Fe/MgO (0 0 1) Films by Controlling Interface 691
Oxide Distribution. *Appl. Surf. Sci.* **2020**, *533*, 147501. 692
- (66) Kons, C.; Phan, M. H.; Srikanth, H.; Arena, D. A.; Nemat, Z.; 693
Borchers, J. A.; Krycka, K. L. Investigating Spin Coupling across a 694
Three-Dimensional Interface in Core/Shell Magnetic Nanoparticles. 695
Phys. Rev. Mater. **2020**, *4*, 034408. 696